AIP Advances

# Propagation-based phase-contrast tomography for high-resolution lung imaging with laboratory sources

Martin Krenkel, Mareike Töpperwien, Christian Dullin, Frauke Alves, and Tim Salditt

Citation: AIP Advances **6**, 035007 (2016); doi: 10.1063/1.4943898
View online: http://dx.doi.org/10.1063/1.4943898
View Table of Contents: http://scitation.aip.org/content/aip/journal/adva/6/3?ver=pdfcov
Published by the AIP Publishing



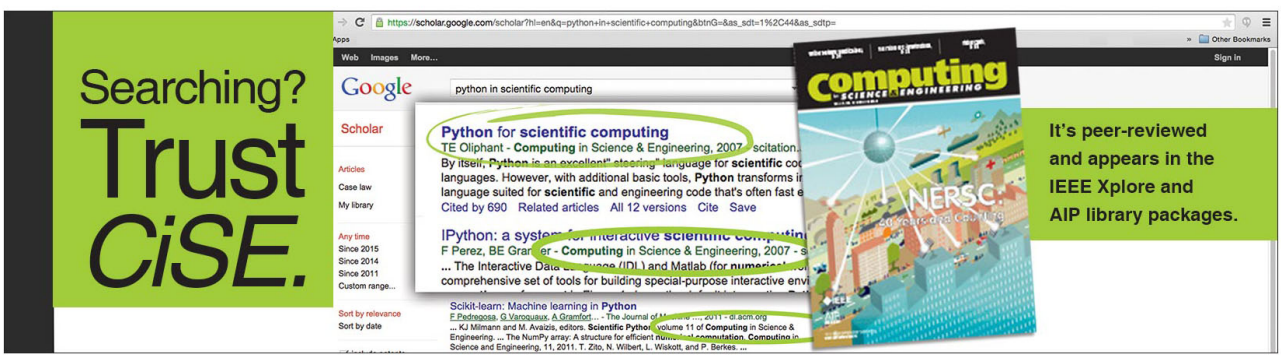

# Propagation-based phase-contrast tomography for high-resolution lung imaging with laboratory sources

Martin Krenkel,[1,a] Mareike Töpperwien,[1] Christian Dullin,[2] Frauke Alves,[2,3,4] and Tim Salditt[1,b]

[1]*Institute for X-Ray Physics, University of Göttingen, 37077 Göttingen, Germany*
[2]*Institute of Diagnostic and Interventional Radiology, University Medical Center Göttingen, 37075 Göttingen, Germany*
[3]*Department of Haematology and Medical Oncology, Medical Center Göttingen, 37075 Göttingen, Germany*
[4]*Department of Molecular Biology of Neuronal Signals, Max-Planck-Institute of Experimental Medicine, 37075 Göttingen, Germany*

(Received 21 October 2015; accepted 29 February 2016; published online 8 March 2016)

We have performed high-resolution phase-contrast tomography on whole mice with a laboratory setup. Enabled by a high-brilliance liquid-metal-jet source, we show the feasibility of propagation-based phase contrast in local tomography even in the presence of strongly absorbing surrounding tissue as it is the case in small animal imaging of the lung. We demonstrate the technique by reconstructions of the mouse lung for two different fields of view, covering the whole organ, and a zoom to the local finer structure of terminal airways and alveoli. With a resolution of a few micrometers and the wide availability of the technique, studies of larger biological samples at the cellular level become possible.  [http://dx.doi.org/10.1063/1.4943898]

Tomographic x-ray imaging is a powerful technique to image interior structures in otherwise opaque specimen. Small-animal imaging by computed tomography is an indispensable tool for biomedical research, achieving a resolution down to a few micrometers with state-of-the-art scanners. However, as the technique is based on the weak absorption interaction of x-rays with matter, contrast vanishes for weakly absorbing tissues, in particular at small scales. Hence, many relevant small structural details remain elusive. The lung presents a perfect example for an important tissue structure, which cannot be visualized in the whole animal at cellular resolution. To circumvent this limitation, x-ray phase contrast was introduced two decades ago using highly brilliant synchrotron sources.[1–3] In the complex index of refraction, which for hard x-rays is conventionally written as $n = 1 - \delta + i\beta$, the decrement $\delta$ is up to three orders of magnitude larger than the extinction coefficient $\beta$. Hence, relative changes $\Delta\delta$ and $\Delta\beta$ to the surrounding material, resulting in phase and absorption contrast, respectively, are also much larger. Therefore, contrast and resolution for soft tissue can potentially be strongly improved by turning to phase-contrast tomography.

A widely used technique to achieve phase contrast in biomedical imaging is based on the Talbot and Talbot-Lau effects, using a set of diffraction gratings to extract the gradient of the phase in the sample's exit plane.[4,5] Importantly, grating interferometry can be implemented at low-brilliance sources that are readily available in the laboratory.[6–8] Notwithstanding its uncontested merits for large specimen, this technique, however, is limited in resolution by the grating period, a precise alignment of the gratings, and requires relatively high monochromaticity.[9] Moreover, the increased dose due to finite diffraction efficiencies, scanning of gratings, and absorption in the analyzer grating may pose a challenge for radiation sensitive applications. Contrarily, (lensless) techniques

[a]Corresponding author, mkrenke@gwdg.de
[b]tsaldit@gwdg.de

 

without optical elements between object and detector such as propagation-based phase contrast are intrinsically more dose efficient.[10,11] In addition, propagation-based phase contrast is compatible with a much lower degree of partial coherence.[12] The invention of high-brilliance micro-focus sources, which are based on a liquid-metal anode instead of a solid target, has now paved the way to enable phase-contrast imaging in the laboratory.[13–15]

The lung structure is an excellent example of how the 3D structure is related to biological function. Therefore, its 3D imaging is an important application of tomography and recent technological developements have enabled lung studies of small animals by employing grating-based contrast mechanisms.[16,17] However, high-resolution studies have so far been limited to excised and / or dried lungs[18,19] that are far from *in vivo* conditions. In this work we have used propagation-based phase-contrast tomography to image the *in situ* 3D structure of mouse lungs in whole animals. Two-dimensional phase-contrast imaging on whole mice was recently enabled by employing liquid-metal-jet x-ray sources.[20] Here, we extend this technique towards phase-contrast tomography and we show that phase-retrieval is necessary to obtain meaningful reconstruction values, which can be used for automated analysis and rendering. Enabled by the unprecedented data quality, local tomography is sucessfully demonstrated for a small region of interest (ROI), exhibiting the potential of in-line holographic phase-retrieval for small-animal imaging at a (half-period) resolution of about 5 μm.

For propagation-based phase-contrast imaging in paraxial approximation, the Fresnel number $F = \frac{a^2}{\lambda z_{\text{eff}}}$, with a typical lateral dimension $a$, the wavelength $\lambda$ and the effective propagation distance $z_{\text{eff}} = z_{01} \cdot (z_{02} - z_{01})/z_{02}$ controls the image formation.[21,22] Especially for $F \approx 1$, images are in the direct-contrast regime, showing pronounced edge enhancement, which can be described, e.g., by the Transport of Intensity equation (TIE).[23,24] Assuming a single material and short propagation distances, this equation can be solved for the object phase-distribution $\phi(\mathbf{r}_\perp, 0)$ using pseudo differential operators[25]

$$\phi(\mathbf{r}_\perp, 0) = \frac{\kappa}{2} \cdot \ln \mathcal{F}_\perp^{-1} \left( \frac{\mathcal{F}_\perp \left( I(\mathbf{r}_\perp, \Delta z)/I_0 \right)}{\left( \frac{\kappa}{4\pi F^1} \left| \mathbf{k^0}_\perp \right|^2 + 1 \right)} \right), \tag{1}$$

with the normalized phase-contrast image $I(\mathbf{r}_\perp, \Delta z)/I_0$, the dimensionless spatial frequencies $\mathbf{k}^0_\perp$ of the lateral Fourier transform $\mathcal{F}_\perp$, the ratio $\kappa = \delta/\beta$ of decrement and extinction coefficient of the refractive index, and the Fresnel number $F^1$ for a lateral size $a$ corresponding to one pixel. In practice, the ratio $\kappa$ is chosen based on visual inspection. A second phase-retrieval approach used in this work, known as Bronnikov Aided Correction (BAC), is based on reconstructing an approximate phase distribution $\phi^\dagger$ similar to Eq. (1) and to subsequently obtain corrected images by[26]

$$I_a(\mathbf{r}_\perp) = \frac{I(\mathbf{r}_\perp, \Delta z)}{1 - \gamma \nabla_\perp^2 \phi^\dagger(\mathbf{r}_\perp)}, \tag{2}$$

where physical parameters have been replaced by the visually inspected parameter $\gamma$ and $\nabla_\perp^2$ denotes the 2D Laplacian. Tomographic reconstructions were performed using a cone-beam reconstruction algorithm (Bronnikov Algorithms, The Netherlands) and local tomography data is smoothly extended by replicating boundary pixel values to avoid artifacts from interior tomography.

Whole mice were prepared following the protocol for *ex vivo* experiments described earlier.[27] Wild type mice were sacrificed using an isoflurane overdose and the collapsing lung was inflated with air, using a constant pressure of 30 cm water column. The trachea was subsequently tied up and the mice were embedded in a tube with 1% agarose gel, mounted on a holder, as shown in Fig. 1(a). Tomographic scans were recorded using a self-built cone-beam tomography instrument equipped with a liquid-metal x-ray source (JXS D2, Excillum, Sweden),[28] operated at 70 kV acceleration voltage. Due to the liquid state of the anode material in the jet and its continuous replenishment, the power density of the focused electron spot has been increased by a factor of 10 with respect to conventional microfocus x-ray sources.[28] The source is operated with Galinstan, an alloy being liquid at room temperature, in which characteristic $K_\alpha$ radiation is generated at 9.25 keV ($Ga$), 24.2 keV ($In$), and 25.3 keV ($Sn$), superimposed on the bremsstrahlung spectrum. The $Ga$ line dominates based on the composition of the alloy, but is too low in photon energy for experiments

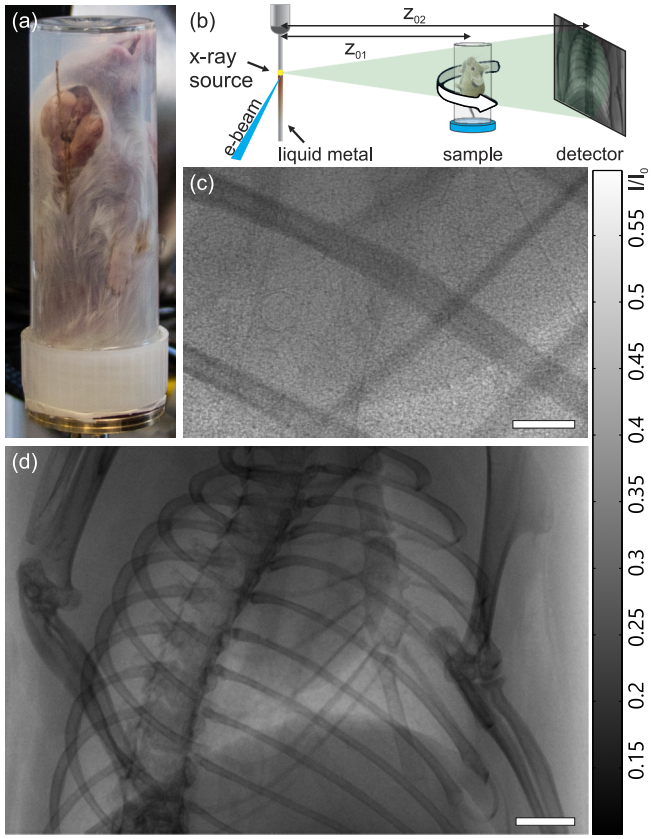


FIG. 1. (a) Photograph of the sample mounted in the experimental setup. (b) Sketch of the setup: X-rays are generated in a small spot on a liquid-metal-jet producing a divergent x-ray beam. By moving the detector or the sample, different geometric magnifications can be achieved. (c) Projection of the large-FOV dataset that covers the whole mouse, showing mostly absorption contrast. (d) Phase-contrast projection obtained by moving the detector farther away ("zoom-move"), leading to a measurement in a ROI indicated by the dashed rectangle in (c). Aside from the expected increase in magnification, also pronounced edge enhancement around soft tissue structures is observed. Scalebars denote 2 mm in (c) and 400 μm in (d).

performed on whole mice. Previous approaches had the goal of using a different alloy, which however has to be preheated to be in the molten state.[20] Here, we used optimized spectral filters (see Table I) to single out the high-energy lines of the conventional alloy. Specimen were mounted on a fully motorized sample tower with adjustable rotation axis. By choosing the source-to-rotation axis and the detector distance, different magnifications can easily be achieved due to the cone-beam geometry of the experimental setup, depicted in Fig. 1(b). Tomographic projection data was acquired using a photon-counting detector based on the Timepix chip (XIE, Germany) with a pixel size of 55 μm and an indirect x-ray camera (sCMOS with 15 μm gadox, Photonic Science, UK) with 6.5 μm pixel size (resampled to 13 μm).

Figure 1 shows typical projections of a mouse recorded in a setting with large field of view (large-FOV) (c) and at larger magnification (d), obtained by moving the detector farther away (zoom-move setting). The dashed area in (c) indicates the region that is recorded at higher resolution. Due to the smaller Fresnel number $F$[1], phase-contrast effects can be observed especially for fine lung structures in the zoom setting. Alternatively, phase-contrast projections can be obtained by employing a high-resolution detector, which results in even smaller Fresnel numbers, again enabling phase-contrast measurements. This setting will be denoted as zoom-detector. Tomographic measurements were carried out in the three different experimental settings, with parameters detailed in Table I.

Figure 2 shows reconstructed orthoslices of the high-resolution measurements of the lung for the zoom-move setting, shown in (a) and (b), and for the zoom-detector setting in (c) and (d). In both cases the left column (a,c) shows the tomographic reconstruction without any phase-retrieval

TABLE I. Experimental parameters for the three datasets shown. Exposure time denotes the time for each projection. Filter foils are a 25 µm thick nickel foil (Ni) and a 35 µm thick silver foil (Ag). Dose values are calculated for a model protein ($\rho = 1.35\,\mathrm{g/cm^3}$) with weighted spectral contributions.

| | large-FOV | zoom-move | zoom-detector |
|---|---|---|---|
| $z_{01}$ | 0.24 m | 0.15 m | 0.15 m |
| $z_{02}$ | 0.44 m | 1.53 m | 0.37 m |
| pixel size | 55.0 µm | 55.0 µm | 13 µm |
| voxel size | 29.9 µm | 5.38 µm | 5.26 µm |
| $F^1$ | 120 | 1.59 | 0.57 |
| angular steps | 916 | 995 | 916 |
| angular range | 183° | 360° | 360° |
| exposure time | 0.8 s | 10 s | 10 s |
| source size | $(40\times10)\,\mu m^2$ | $(40\times10)\,\mu m^2$ | $(20\times5)\,\mu m^2$ |
| x-ray power | 100 W | 100 W | 40 W |
| filters used | Ni | Ni | Ni + Ag |
| total dose | 7.2 Gy | 246.0 Gy | 26.4 Gy |

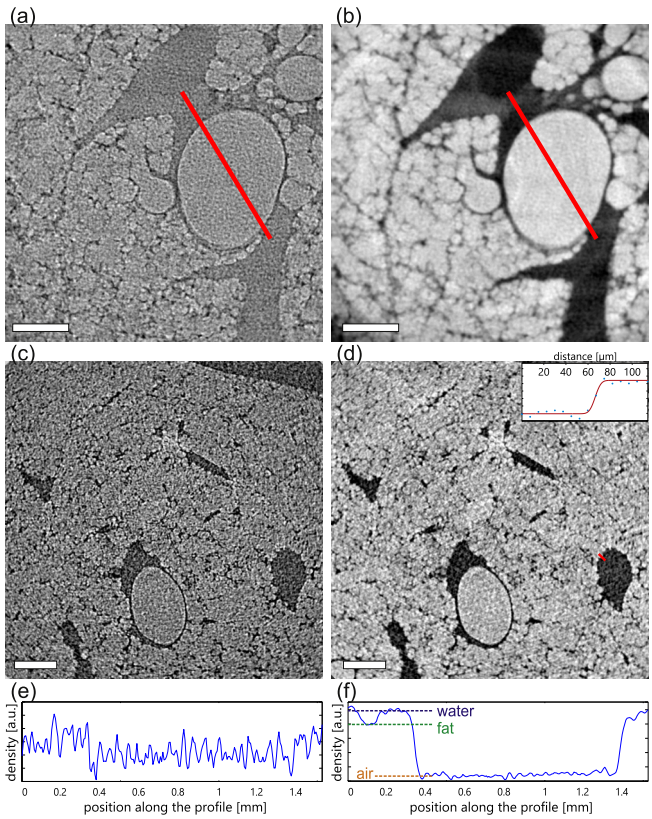


FIG. 2. The benefit of phase retrieval illustrated by exemplary slices through the 3D reconstruction volume: The left column shows orthoslices without application of any phase retrieval. The right column shows the same orthoslices, but with phase retrieval performed prior to tomographic reconstruction. (a,b) Orthoslices obtained in the "zoom-move" setting, where the sample-detector distance was increased to obtain phase contrast. (c,d) Orthoslices obtained in the "zoom-detector" setting, where a high resolution detector was used to decrease the Fresnel number. The inset shows the reconstructed values along the red line with an error function fit with 9.8 µm FWHM. (e,f) Profiles through the reconstructed volume obtained along the 6 pixel wide line, as indicated by the red lines in (a) and (b). All scalebars denote 500 µm.

algorithm applied. Typical edge-enhancement effects can be observed at the boundary between air and soft tissue, clearly indicating the presence of phase contrast. Although anatomical structures can be identified by eye, the profile function shown in Fig. 2(e) (taken along the red line in Fig. 2(a)) shows barely any differences between the different materials (e.g. between air and soft tissue). Phase retrieval was performed using the Paganin method (Eq. (1)) and the BAC algorithm (Eq. (2)) for the reconstruction in Fig. 2(b) and 2(d), respectively, yielding quantitative density maps, in which darker values correspond to a higher electron density. The values along the same profile as before that are plotted in Fig. 2(f) now show significantly different density levels, which can be used to distinguish water, fat and air. This enables automatic density-based segmentation and 3D rendering of the reconstructed volume.

Measurements of a test pattern (RT RC-02B, JIMA, Japan) reveal a half-period resolution of $2 \times 3\,\mu m^2$ (h × v) in a similar geometry with effective pixel sizes chosen small enough. However, if very small structures in the zoom-move reconstruction are regarded, doubling and blurring of fine structures are observed, which we attribute to motion artifacts. Contrarily, the resolution of the reconstruction in Fig. 2(c) and 2(d) is only limited by the pixel size as confirmed by calculations of the Fourier-shell correlation (FSC). Further, the line scan over a boundary between air and water reveals an edge spread function with 9.8 μm full width at half maximum (FWHM) and alveoli with approximately 20 μm diameter can be found, which confirms the high resolution. We attribute this absence of motion artifacts to the additional filter that was used in this scan. Not only the overall dose was significantly reduced, but in particular the combination of the *Ag* and *Ni* filters removes a residual low-energy peak in the x-ray spectrum, as illustrated in the supplementary material.[29] Interestingly, the application of the BAC algorithm resulted in streak artifacts in the zoom-move dataset so that instead the Paganin method was used for phase retrieval, which suffices to suppress the streaks. In the dataset without motion artifacts, no streak artifacts are observed. Hence, it is reconstructed with the BAC algorithm, allowing for a higher resolution.[26]

Figure 3 shows an orthoslice of the large-FOV dataset (a) together with a 3D rendering of the thorax (b), consisting of an automatic segmentation of the bone (gray), the lung structure (pink) and a manually segmented region of the heart (red). The dashed rectangle indicates the region covered by the high-resolution scan in the zoom-move setting. The inset in (a) shows a magnification of the large-FOV dataset corresponding to the lung slice shown in Fig. 2(a), 2(b). The same structures can be identified in both measurements. Based on visual inspection, the dataset with higher resolution was aligned within the coarser structure of the large-FOV dataset. Enabled by the phase retrieval, an automatic rendering of the zoomed dataset is presented in Fig. 3(c), where the volume rendering is limited to a sub-volume, visualizing a cut through a larger bronchial tube, which branches into smaller bronchioles. The entire 3D structure of the two datasets can be best appreciated by a video, supplied as online material.

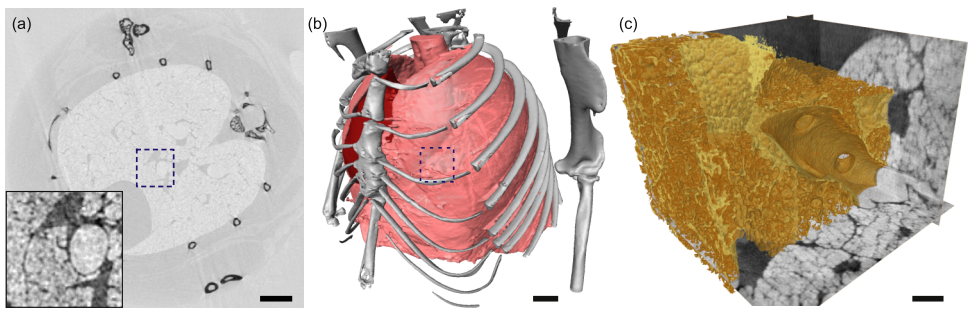


FIG. 3. (a) Orthoslice perpendicular to the rotation axis of the "large FOV" tomographic reconstruction. The inset shows a zoom into the lung area marked by the dashed rectangle with adjusted contrast. (b) 3D rendering of the "large FOV" volume showing the thorax, containing automatically segmented bones (gray), the heart (red) and lung tissue (pink). The dashed area denotes the region shown in the inset in (a). (c) 3D rendering of the "zoom-move" dataset (see Fig. 2(c), 2(d)), obtained by tomographic reconstruction of the phase-retrieved projections. Three orthoslices together with a volume rendering of the soft-tissue structure are shown. Scale bars denote 2 mm in (a,b) and 500 μm in (c). (Multimedia view) [URL: http://dx.doi.org/10.1063/1.4943898.1]

In summary we have shown an application of propagation-based phase contrast, which is routinely used for small-animal imaging at synchrotron facilities, with a highly brilliant liquid-metal-jet laboratory source. The use of an optimized energetic spectrum has enabled measurements of whole mice lungs at a (half-period) resolution down to 5 μm, as validated by line scans and FSC calculations. Thus, the precise tracking of labeled cells is enabled, e.g. the location of barium-labeled alveolar macrophages in relation to anatomical structures, as recently demonstrated in synchrotron experiments.[27,30] In contrast to synchrotron radiation, laboratory sources provide a high availability, so that biological studies that typically involve many different samples become possible with this novel technique. Besides trying to use alloys with higher *In* content to increase the high-energy part of the energetic spectrum, current source developments aim at increasing the x-ray power by another order of magnitude.[19,28] This will allow faster acquisition rates so that the presented phase-contrast imaging approach might also be used for high-resolution imaging of living animals in future.

We thank Andrea Markus for help in sample preparation. Financial support by the SFB 755 "Nanoscale photonic imaging" and BMBF-Verbundforschung is gratefully acknowledged.

[1] K. A. Nugent, T. E. Gureyev, D. F. Cookson, D. Paganin, and Z. Barnea, Phys. Rev. Lett. **77**, 2961 (1996).
[2] P. Cloetens, R. Barrett, J. Baruchel, J.-P. Guigay, and M. Schlenker, Journal of Physics D: Applied Physics **29**, 133 (1996).
[3] T. J. Davis, D. Gao, T. E. Gureyev, A. W. Stevenson, and S. W. Wilkins, Nature **373**, 595 (1995).
[4] F. Pfeiffer, O. Bunk, C. David, M. Bech, G. Le Duc, A. Bravin, and P. Cloetens, Phys. Med. Biol. **52**, 6923 (2007).
[5] G. Schulz, T. Weitkamp, I. Zanette, F. Pfeiffer, F. Beckmann, C. David, S. Rutishauser, E. Reznikova, and B. Müller, J. R. Soc. Interface **7**, 1665 (2010).
[6] F. Pfeiffer, T. Weitkamp, O. Bunk, and C. David, Nat. Phys. **2**, 258 (2006).
[7] A. Tapfer, R. Braren, M. Bech, M. Willner, I. Zanette, T. Weitkamp, M. Trajkovic-Arsic, J. T. Siveke, M. Settles, M. Aichler, A. Walch, and F. Pfeiffer, PLoS ONE **8**, e58439 (2013).
[8] T. Thüring, T. Zhou, U. Lundström, A. Burvall, S. Rutishauser, C. David, H. M. Hertz, and M. Stampanoni, Applied Physics Letters **103**, 091105 (2013).
[9] I. Zanette, S. Lang, A. Rack, M. Dominietto, M. Langer, F. Pfeiffer, T. Weitkamp, and B. Müller, Appl. Phys. Lett. **103**, 244105 (2013), http://dx.doi.org/10.1063/1.4848595.
[10] T. Zhou, U. Lundström, T. Thüring, S. Rutishauser, D. H. Larsson, M. Stampanoni, C. David, H. M. Hertz, and A. Burvall, Opt. Express **21**, 30183 (2013).
[11] M. Bartels, M. Krenkel, J. Haber, R. N. Wilke, and T. Salditt, Phys. Rev. Lett. **114**, 048103 (2015).
[12] D. Paganin and K. A. Nugent, Phys. Rev. Lett. **80**, 2586 (1998).
[13] T. Tuohimaa, M. Otendal, and H. M. Hertz, Appl. Phys. Lett. **91**, 074104 (2007).
[14] M. Bartels, V. H. Hernandez, M. Krenkel, T. Moser, and T. Salditt, Appl. Phys. Lett. **103**, 083703 (2013).
[15] I. Zanette, T. Zhou, A. Burvall, U. Lundström, D. H. Larsson, M. Zdora, P. Thibault, F. Pfeiffer, and H. M. Hertz, Phys. Rev. Lett. **112**, 253903 (2014).
[16] S. Schleede, F. G. Meinel, M. Bech, J. Herzen, K. Achterhold, G. Potdevin, A. Malecki, S. Adam-Neumair, S. F. Thieme, F. Bamberg, K. Nikolaou, A. Bohla, A. Ā. Yildirim, R. Loewen, M. Gifford, R. Ruth, O. Eickelberg, M. Reiser, and F. Pfeiffer, PNAS **109**, 17880 (2012), http://www.pnas.org/content/109/44/17880.full.pdf.
[17] A. Yaroshenko, F. G. Meinel, M. Bech, A. Tapfer, A. Velroyen, S. Schleede, S. Auweter, A. Bohla, A. Ā. Yildirim, K. Nikolaou, F. Bamberg, O. Eickelberg, M. F. Reiser, and F. Pfeiffer, Radiology **269**, 427 (2013), pMID: 23696682, http://dx.doi.org/10.1148/radiol.13122413.
[18] D. M. Vasilescu, C. Klinge, L. Knudsen, L. Yin, G. Wang, E. R. Weibel, M. Ochs, and E. A. Hoffman, J. Appl. Physiol. **114**, 716 (2013), http://jap.physiology.org/content/114/6/716.full.pdf.
[19] D. Larsson, Small-Animal Imaging with Liquid-Metal-Jet X-ray Sources, Ph.D. thesis, KTH Royal institute of technology, 2015.
[20] D. H. Larsson, U. Lundström, U. K. Westermark, M. Arsenian Henriksson, A. Burvall, and H. M. Hertz, Medical Physics **40**, 021909 (2013).
[21] D. M. Paganin, *Coherent X-Ray Optics* (Oxford University Press, New York, 2006).
[22] M. Krenkel, M. Töpperwien, M. Bartels, P. Lingor, D. Schild, and T. Salditt, Proc. SPIE **9212**, 92120R (2014).
[23] M. R. Teague, J. Opt. Soc. Am. **73**, 1434 (1983).
[24] M. Krenkel, M. Bartels, and T. Salditt, Opt. Express **21**, 2220 (2013).
[25] D. Paganin, S. C. Mayo, T. E. Gureyev, P. R. Miller, and S. W. Wilkins, J. Microsc. **206**, 33 (2002).
[26] Y. D. Witte, M. Boone, J. Vlassenbroeck, M. Dierick, and L. V. Hoorebeke, J. Opt. Soc. Am. A **26**, 890 (2009).
[27] C. Dullin, S. dal Monego, E. Larsson, S. Mohammadi, M. Krenkel, C. Garrovo, S. Biffi, A. Lorenzon, A. Markus, J. Napp, T. Salditt, A. Accardo, F. Alves, and G. Tromba, J. Synchrotron Rad. **22**, 143 (2015).
[28] M. Otendal, T. Tuohimaa, U. Vogt, and H. M. Hertz, Rev. Sci. Instrum. **79**, 016102 (2008).
[29] See supplementary material at http://dx.doi.org/10.1063/1.4943898 for measurements of the energetic spectrum.
[30] M. Krenkel, A. Markus, M. Bartels, C. Dullin, F. Alves, and T. Salditt, Sci. Rep. **5** (2015).